RSC Advances

PAPER

View Article Online
View Journal | View Issue

Check for updates

Cite this: *RSC Adv.*, 2025, **15**, 27063

Fast and sensitive analysis of explosive compounds using Co_3O_4–MnO_2@MWCNTs nanocomposite integrated electrochemical sensing platform†

Mohamed F. El-berry,[bc] Ahmed M. Abdalla,[c] Mohamed S. Attia *[b] and Rabeay Y. A. Hassan *[a]

Fast and accurate determination of toxic and explosives compounds are necessary. Thus, a portable-electrochemical sensing system was developed for the rapid and sensitive detection of 2,4,6-trinitrotoluene (TNT) using a screen-printed electrode (SPE) modified with a Co_3O_4/MnO_2@MWCNTs nanocomposite. This nanocomposite combines the electrocatalytic activity of the hybrid metal oxides (Co_3O_4 and MnO_2) with the high conductivity and surface area of multi-walled carbon nanotubes (MWCNTs), resulting in enhanced sensor performance. The modified SPE exhibited excellent electrocatalytic activity towards TNT voltammetric reduction, showing a well-defined voltammetric response. Electrochemical characterization using cyclic voltammetry (CV) and electrochemical impedance spectroscopy (EIS) demonstrated the improved electron transfer kinetics and reduced charge transfer resistance at the modified electrode. Differential pulse voltammetry (DPV) was employed for quantitative TNT detection, achieving a linear response in the concentration range of 0.33 to 50 ppm with a detection limit of 0.153 ppm. The sensor demonstrated good selectivity against common interferents and other nitroaromatic compounds. Furthermore, the newly developed sensor surface exhibited satisfactory stability and reproducibility, making it a promising candidate for on-site and real-time TNT detection in environmental and security applications.

Received 29th May 2025
Accepted 14th July 2025

DOI: 10.1039/d5ra03807c

rsc.li/rsc-advances

Open Access Article. Published on 29 July 2025. Downloaded on 2/19/2026 11:39:10 AM.
This article is licensed under a Creative Commons Attribution-NonCommercial 3.0 Unported Licence.

1. Introduction

In recent years, terrorism has risen significantly, with explosives being the weapon of choice in most attacks due to their ease of use, straightforward deployment, and destructive potential.[1] To address the escalating threat, it is crucial to develop effective and reliable techniques for detecting high-explosive compounds that are usually utilized in such attacks, including picric acid (2,4,6-trinitrophenol), PETN (pentaerythritol tetranitrate), RDX (cyclotrimethylene trinitramine), and the TNT (2,4,6-trinitrotoluene).

Detecting these explosives, even at trace levels, in vehicles, luggage, mail, aircraft, and soil, is vital for enhancing public safety and security.[2] Aromatic and/or aliphatic nitro-containing compounds are the explosive reactive-agents that are widely used in military applications. In this regard, NO_2-groups, involved as the oxidizing initiator due its strong electron-trapping features, lead the extremely fast and highly exothermic chemical reactions. Accordingly, rapid expansion of matter due to the strong release of gases and emitted heat is occurring prior to the explosion. Hence, NO_2-based compounds are very sensitive to the influence of heat, shocks, and frictions.[3]

Trinitrotoluene (TNT) is one of the most widely used nitro-aromatic explosives in both military and civilian sectors, historically and at present.[4] The TNT has significant toxic effects on human health and the environment. It can persist in soil and water for long periods, leading to contamination of ecosystems. It can inhibit plant growth, reduce seed germination rates, and cause root damage. Plants absorb TNT from the soil, which can affect their metabolic processes and stunt growth. TNT can leach into groundwater from contaminated soils or through surface water bodies, posing a risk to drinking water supplies.[5]

Therefore, human health is at danger from exposure to TNT-contaminated water, particularly in areas where drinking water is derived from surface or groundwater. According to the US Environmental Protection Agency (US-EPA), TNT is listed as one of the main toxic compounds that may exert a great impact on humans and environment. If exposure occurs over long periods of time, it can have harmful and carcinogenic effects on humans, leading to problems like skin irritation, liver damage, and other long-term health difficulties.[6]

[a]*Biosensors Research Lab, Zewail City of Science and Technology, 6th October City, Giza 12578, Egypt. E-mail: ryounes@zewailcity.edu.eg*

[b]*Chemistry Department, Faculty of Science, Ain shams University, Abbassia, Cairo 11566, Egypt. E-mail: Mohamed_sam@yahoo.com*

[c]*Military Technical Research Centre, Cairo, Egypt*

† Electronic supplementary information (ESI) available. See DOI: https://doi.org/10.1039/d5ra03807c

© 2025 The Author(s). Published by the Royal Society of Chemistry

Open Access Article. Published on 29 July 2025. Downloaded on 2/19/2026 11:39:10 AM. This article is licensed under a Creative Commons Attribution-NonCommercial 3.0 Unported Licence.

Therefore, one of the most important analytical challenges is the development of sensitive and selective techniques for the detection and measurement of nitroaromatics compounds in general, and TNT especially.[7] Currently, various commercial devices are available for detecting TNT such as gas-chromatography-mass spectrometry (GC-MS), ion mobility spectroscopy (IMS),[8,9] and metal detectors.[10,11] However, low-sensitivity towards targeting explosive compounds (does not reach the trances levels) is acquired by the metal detectors. In spite of the high sensitivity of analysis provided by the GC-MS and IMS methods, they are cabinet-sized devices, essential calibrations are needed from time-to-time and longtime of analysis, high cost and many expenses for each sample analysis, specific-precautions and long pre-treatments are always required. Thus, those instrumental-based analyses are not highly recommended and they cannot support the onsite and direct detections. Hence, new monitoring (surveillance) systems are needed to support the quick analysis, portability, and low-cost of detection of trace levels of nitro-aromatics.

There are numerous methods for detecting TNT, including Raman spectrometry,[12–14] photoluminescence,[15–17] and High-Performance Liquid Chromatography (HPLC).[18–20] These conventional techniques for TNT detection are problematic for field use since they frequently call for expensive equipment, time-consuming sample preparation, and skilled handling.

For quick, affordable, and portable devices, electrochemical sensors, particularly those built on screen-printed electrodes, offer a potential alternative.[21,22] Electrochemical sensors rely on measuring the electrical signals generated by the redox reactions of analytes, such as the redox reactions of TNT at the sensor surface. These sensors are often highly sensitive with very low detection limits, and selective, allowing them to differentiate between similar compounds.[23] SPEs are particularly advantageous in sensor technology due to their low cost, disposability, and ease of fabrication. These can be modified with nanomaterials like metal oxides and carbon-based structures to enhance their electrochemical activity and sensitivity.[24–26] In terms of TNT-redox behaviors, there are three major distinguished cathodic (voltammetric) peaks usually detected upon the electrochemical reduction of the active three-nitro groups in the TNT compounds. Thus, steps of mechanisms behind this voltammetric TNT-reaction (*i.e.* the steps of the cathodic reaction of the three-nitro groups) are well known and well studied in aqueous electrolytes. A total of 18-protons (H^+), 18-electrons (e^-) are generally transferred attributed to the 6-protons along with 6-electrons for each reduction step.[27]

In recent advancements, incorporating nanocomposites such as cobalt oxide (Co_3O_4), manganese oxide (MnO_2), and multi-walled carbon nanotubes (MWCNTs) into the electrode structure has further improved the sensor performance. These materials contribute unique properties: Co_3O_4 and MnO_2 enhance electrocatalytic activity, while MWCNTs increase the surface area and conductivity, facilitating efficient electron transfer. Hence, such a combination enables the sensor to rapidly detect low concentrations of TNT with high accuracy. By leveraging the unique properties of nanocomposites on SPEs, electrochemical sensors have become a promising platform for reliable and on-site TNT detection, addressing the needs in environmental safety, security, and defense applications.

2. Experimental

2.1. Materials and reagents

2,4,6-trinitrotoluene (TNT) and 2,4-dinitrotoluene (DNT) were purchased from Abu-Zaabal company for specialty chemicals, Cairo, Egypt. Nitrobenzene (NB) and phosphoric acid (85%) were purchased from Sigma Aldrich. Manganese oxide (MnO_2), tungsten oxide (WO_3), cobalt oxide (Co_3O_4), lanthanum oxide (La_2O_3), aluminum oxide (Al_2O_3), nickel oxide (NiO) in addition to the multi-walled carbon nanotubes (MWCNTs) were screened for the selection of the highest reduction peak current of nitro-aromatic group. The nanomaterials were prepared at the concentration of 5.0 mg mL^{-1} for metal oxides and 2.0 mg mL^{-1} for MWCNTs. A 10 mM potassium phosphate buffer was prepared from K_2HPO_4 and adjusted to pH 6.5 with H_3PO_4. 10 mM of ($K_3[Fe(CN)_6]$) were used for the electrochemical characterization of modified electrodes using the CV and EIS. HPLC grade extra pure acetonitrile was used to prepare the explosives stock solutions, purchased from Sigma Aldrich. Standard solutions of explosives (1.0 mg mL^{-1} in CH_3CN) were prepared carefully in a ventilating hood. All the aqueous solutions were prepared with distilled water at 25 °C. Caution: TNT is highly explosive and should be used cautiously; therefore, all necessary precautions were taken into consideration.

2.2. Electrochemical measurements

Firstly, printed electrodes modified with nanomaterials were activated electrochemically in a pure supporting electrolytes (PBS (pH 7.4)) through running three-consecutive voltammetric sweeping from +0.2 to −1.0 V (*vs.* the silver reference electrode) and under the scan rate of 50 mV s^{-1}. Electrochemical investigations were performed using Palmsens-4 electrochemical portable-potentiostat from Palm-Sense Company (Randhoeve, Netherlands). EIS, and CV analysis were carried out using potassium ferricyanide ($K_3[Fe(CN)_6]$) (10 mM) as the standard redox mediator. EIS-impedimetric measurements were carried out for nanomaterial screening and characterization at a frequency ranging from 10 kHz to 0.1 Hz, 10 mV AC-potential magnitude, and an open circuit potential. Differential pulse voltammetry (DPV) measurements were conducted with the following parameters: step potential = 10 mV, amplitude = 200 mV and pulse width = 20 ms. All electrochemical studies were operated at lab temperature (25 ± 2.0 °C).

2.3. Modification of screen-printed electrodes with the nanocomposite

Individual aqueous suspensions of each nanostructured materials (Co_3O_4, MnO_2 and MWCNTs) were prepared with the concentration of 5.0 mg mL^{-1} (for each metal oxide) and 2.0 mg mL^{-1} (for the carbon nanotubes) and sonicated for 20 minutes (in double-distilled water) to ensure a homogenous dispersion. Then, dispersions of carbon nanotube/bi-metal oxides nanocomposites were formed through mixing a certain volume of

 © 2025 The Author(s). Published by the Royal Society of Chemistry

Open Access Article. Published on 29 July 2025. Downloaded on 2/19/2026 11:39:10 AM.
This article is licensed under a Creative Commons Attribution-NonCommercial 3.0 Unported Licence.

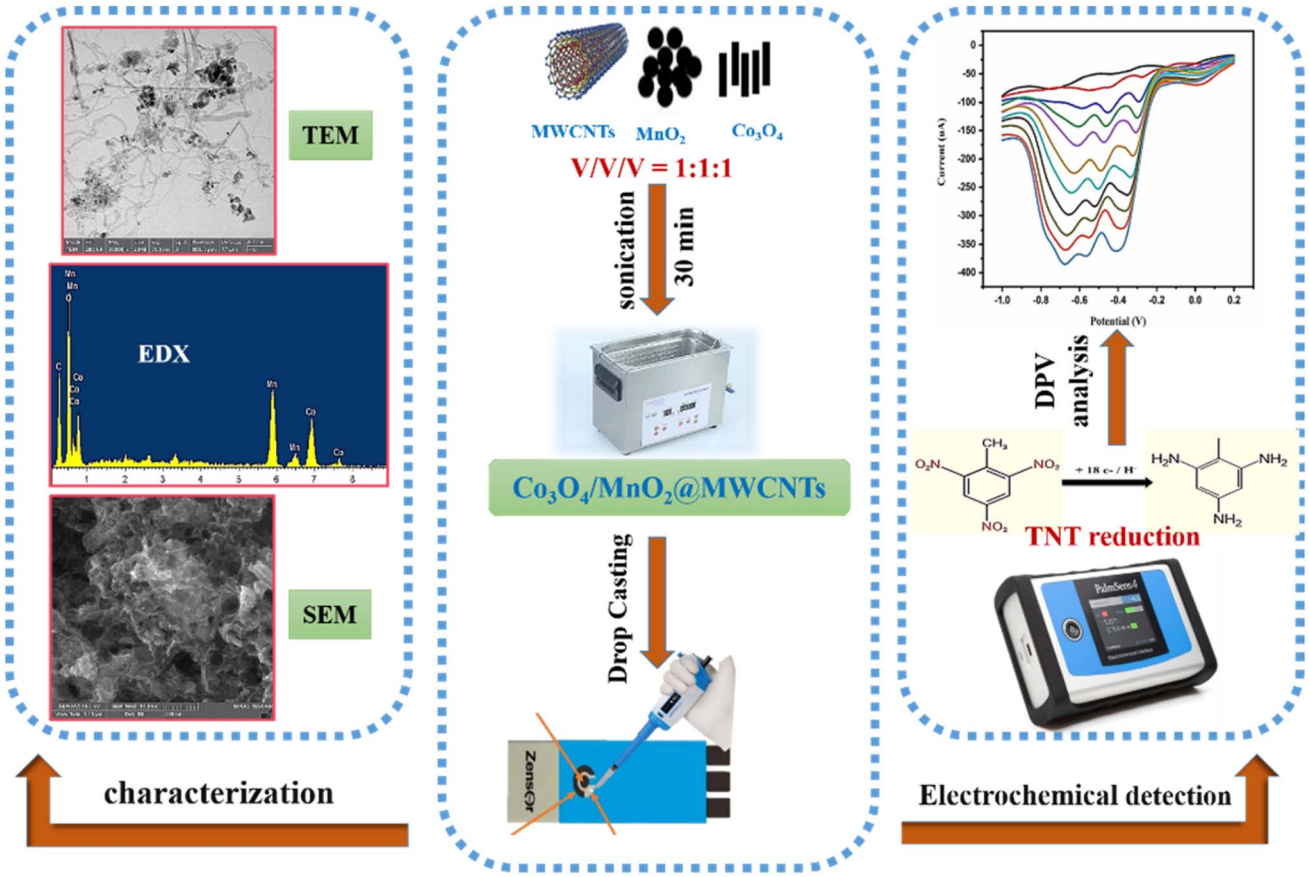

Scheme 1 Surface morphology characterization of nanomaterials; steps of preparation and electrode modifications with the nanocomposite; and the voltammetric detection of TNT using a portable and disposable sensing platform.

MnO_2/Co_3O_4 with the suspension of MWCNTs at the final ratio (1 : 1 : 1). Another 20-min sonication process was conducted to yield the desired nanocomposite. Afterwards, surfaces of printed electrodes were modified *via* drop casting of 10 μL from each of the formed dispassion, and allowed to dry at room temperature. The newly designed TNT-based sensor (steps of fabrication) are highlighted in Scheme 1.

2.4. Nanomaterial characterizations

Surface morphology of modified screen-printed electrodes was investigated using a scanning electron microscope-equipped with an energy-dispersive X-ray spectrometer (EDS spectrometer, SEM, MIRA III XMU, TESCAN). 2D-particle size determination was carried out using the transmission electron microscope (HR-TEM, GEOL F200). Simple sample preparation for the TEM imaging was taken by dispersing and sonicating the nanocomposite materials in an absolute ethanol. Then, a few microliters of each suspension was placed onto a copper grid and left to dry, whereas the operating voltage was 200 KV. Elemental composition analysis for the nanomaterials was obtained using the X-ray photoelectron spectroscopy (XPS, Thermo-Fisher Scientific, K-ALPHA) with a narrow spectrum of 50 eV, a pass energy of 200 eV (full spectrum), pressure of 10–9 mbar, 400 μm spot size, and monochromatic X-ray Al–K-alpha radiation ($h\nu$ = 1350 eV). Eventually, FTIR analysis was conducted using a spectrometer (model Nicolet iS10 from the Thermo-Scientific), whereas all FTIR-spectra were recorded at a range of 4000–400 cm^{-1}.

2.5. Real sample preparation

Electrochemical performance of the newly developed sensing platform was applied for the real detection of targeting analyte (TNT) in real samples. Thus, four different samples (tap water, ground water, sand, and soil samples) were collected and pretreated before determination of the nitro-aromatic group in their content. No special pretreatment was made for water samples, while the supernatant was collected and diluted three-times with the PBS buffer.

For sand and soil samples analysis, two grams of each solid sample were weighed and then grind into fine particles. Subsequently, the fine powder was dispersed in (1.0 mL) acetonitrile. For the convenience of practical operations, the supernatant was collected without filtration and diluted three-times with PBS. TNT (4.97 ppm) was individually spiked into the four real samples. DPV measurements were conducted on each sample (before and after spiking with the known TNT concentration), while the standard addition method was applied to calculate the percentages of recovery with the relative standard deviation (RSD).

Open Access Article. Published on 29 July 2025. Downloaded on 2/19/2026 11:39:10 AM. This article is licensed under a Creative Commons Attribution-NonCommercial 3.0 Unported Licence.

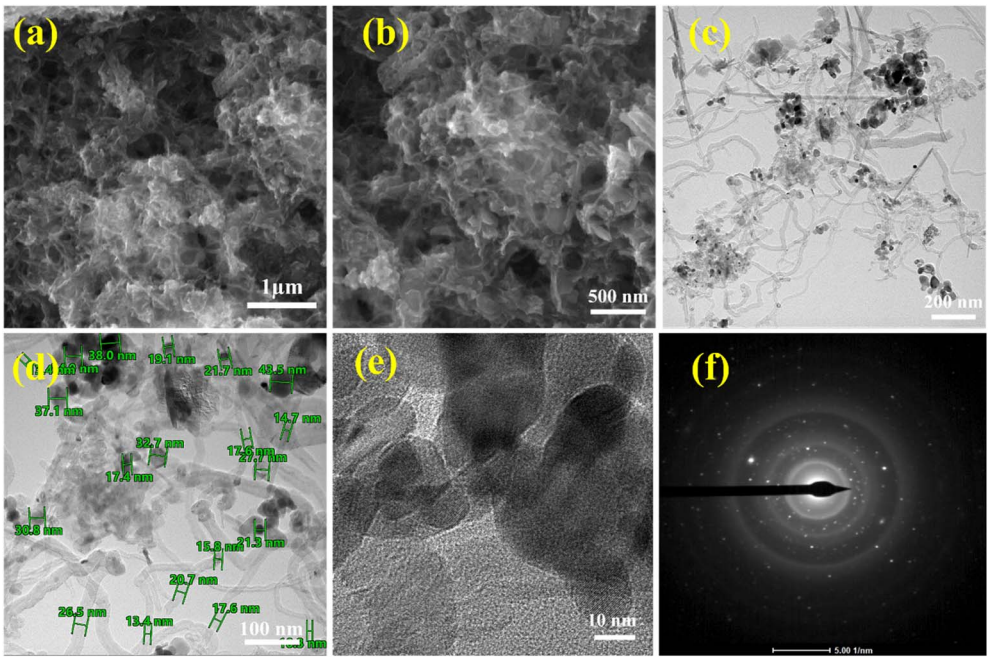

Fig. 1 (a and b) SEM images of nanocomsposites (c and d) TEM images of Co_3O_4–MnO_2@MWCNTs nanocomposite at different magnifications. (e) HRTEM image of Co_3O_4–MnO_2 on MWCNTs. (f) The corresponding diffraction pattern (SAED).

2.6. Data analysis and statistics

The data are presented as the mean ± RSD derived from three independent experiments. Statistical significance was determined through hypothesis testing, with a significance threshold set at $p < 0.05$. The limit of detection (LOD) and limit of quantification (LOQ) were calculated from the given information extracted from the calibration curve. 3.0 × (SD/slope of the curve) used for the LOD determination, while (10 × (SD/slope of the curve)) was used for the LOQ determination. Here, SD refers to the standard deviation of the intercept. All electrochemical results were illustrated in correlated graphs, with the data being evaluated and analyzed using OriginLab software.

2.7. Chemical safety

Nitro-aromatic explosive compounds can lead to anemia, headache, weakness, and liver damage. Prolonged exposure to these chemicals can cause cancer. As these compounds can be readily absorbed through skin, avoiding any direct contact is essential. Stock solutions of these explosives must be handled with extreme caution in a well-ventilated hood. The TNT (solid or liquid forms) must be protected away from any source of heat, oxidizing materials, sheltered from chemical precursors and initiators, and separated from physical frictions and shocking.[28]

3. Results and discussion

3.1. Nanomaterials and sensor surface characterizations

Surface morphology of modified printed electrodes with the nanocomposite (Co_3O_4–MnO_2-MWCNTs) was directly examined with the SEM. In this regard, the SEM images demonstrated well-dispersed and full surface coverage with the nanomaterials, as shown in Fig. 1(a and b). In addition, the light spot of Co_3O_4 and MnO_2 nanoparticles appear to be dispersed on MWCNTs framework, ensuring effective conjugation with the hybrid bi-metal oxide particles.

Consequently, nanostructure characteristics and crystallinity were determined for the nanocomposite using the TEM technique, whereas tubular structures highlighting the carbon nanotube networking were observed, as depicted in Fig. 1(c and e). These elongated connected (non-broken) nanotubes were surrounded (coated) with spherical nanoparticles of the conjugated metal oxides. Moreover, the average size of the nanoparticles was estimated to be between 10.5 and 45 nm, as shown in Fig. 1(d).

Meanwhile, a selected area electron diffraction (SAED) pattern was obtained, as shown in Fig. 1(f). These multiple defined rings of SAED indicated the crystallinity structures of the nanocomposite, which is acquired by manganese oxide and cobalt oxide nanoparticles.

To estimate the individual elemental composition involved in the modification of the SPEs, elemental chemical analysis was performed in the SEM mode using the EDX functions, showing an intensive and uniformed distribution of Co, Mn, C, and O elements on the outer surface of the modified electrodes (Fig. S1, ESI†). The high carbon content validates the incorporation of MWCNTs and the presence of cobalt and manganese peaks, along with oxygen, indicates the existence of cobalt oxide and manganese oxide phase in composite.

Thus, all essential characteristics were provided by the electron microscopic analysis, whereas the formation of the nanocomposite with a homogenous distribution and full

© 2025 The Author(s). Published by the Royal Society of Chemistry

Open Access Article. Published on 29 July 2025. Downloaded on 2/19/2026 11:39:10 AM.
This article is licensed under a Creative Commons Attribution-NonCommercial 3.0 Unported Licence.

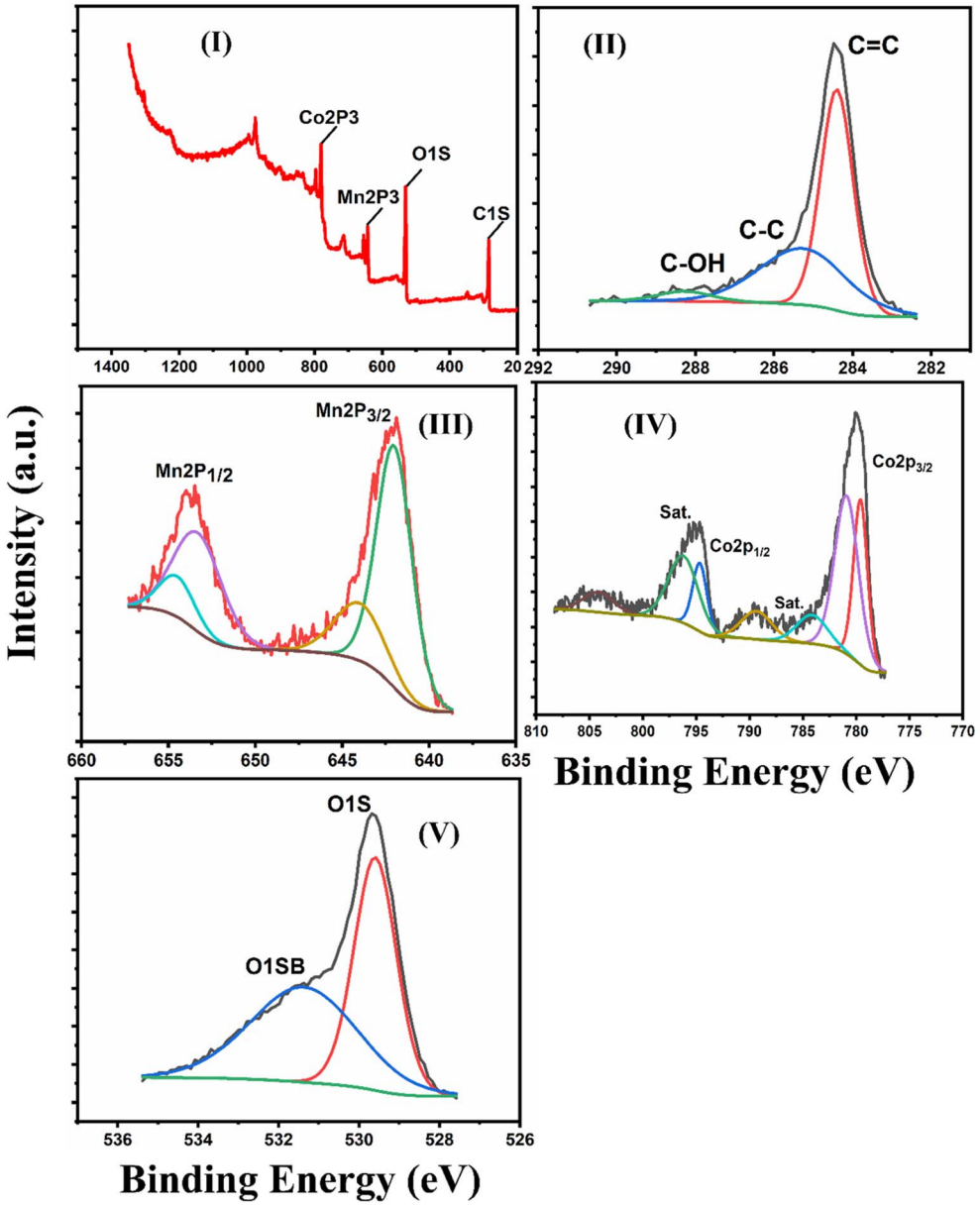

Fig. 2 XPS spectra of the Co_3O_4–MnO_2@MWCNTs nanocomposite: (I) the survey spectrum, (II) O1s, (III) Co2p, (IV) C1s, and (V) Mn2p.

covering on the outer surface of printed electrodes, and their elemental composition. Eventually, XPS analysis was performed to determine the elemental composition and valence states of the entire nanocomposite Co_3O_4–MnO_2@MWCNTs. In this regard, Fig. 2-I demonstrated the complete XPS spectrum obtained for the solid form of the nanocomposite, whereas the major contributed elements (Co, Mn, C, and O) are exhibited from the samples surface analysis. A minor trace of oxygen, and high peak intensity of carbon dedicated at 284.5 eV was the evidence of high purity of the used MWCNTS (Fig. 2-II). Additionally, two strong peaks at the binding energies (642.0 and 653.56 eV) were attributed to the Mn2p3/2 and Mn2p1/2, respectively. Moreover, two peaks with binding energies of 644.0 and 653.71 eV were apportioned to the satellite peaks (Fig. 2-III), confirming the formation of Mn^{4+} and the energy difference ($\Delta E = 11.56$) between both peaks of Mn2p indicated the domination of Mn^{4+} ions in MnO_2.[29] On the other hand, formation of Co_3O_4 phase was confirmed (as shown in Fig. 2-IV), whereas two prominent peaks were collected at the binding energies (779.6 and 795.6 eV) attributed to the $Co2p_{3/2}$, and $Co2p_{1/2}$. This is a proof for the coexistence of Co^{2+} and Co^{3+} in the sample and the two satellite peaks in the spectrum confirmed the presence of a dominant Co_3O_4 phase. Eventually (Fig. 2-V), two additional bands referring to the O1s were recorded at two different binding energy site (529.6, and 531.4 eV) confirming the existence of the typical metal–oxygen bond. With analyzing all given information in Fig. 2, the successful formation of MnO_2–Co_3O_4@MWCNTs nanocomposite is confirmed.

Additionally, FTIR spectroscopy was used to investigate the chemical structures of MWCNTs, Co_3O_4, MnO_2, and the new

© 2025 The Author(s). Published by the Royal Society of Chemistry

Open Access Article. Published on 29 July 2025. Downloaded on 2/19/2026 11:39:10 AM. This article is licensed under a Creative Commons Attribution-NonCommercial 3.0 Unported Licence.

Co_3O_4–MnO_2@MWCNTs nanocomposite composite. The FTIR spectra (Fig. S2, ESI†) confirmed the presence of MWCNTs, Co_3O_4, and MnO_2 with no significant impurities. The composite retains characteristic peaks from its components, with some shifts and intensity variation indicating strong interfacial interactions. These spectral changes confirmed that CNTs serve as the supporting component, enhancing the surface mechanical stability and functionality of Co_3O_4 and MnO_2.

3.2. Electrochemical characterization of the modified electrodes

To develop an efficient sensor platform for the rapid and sensitive electrochemical detection of nitro-aromatic compounds traces in environmental samples, various nanomaterials were characterized and evaluated using the CV and EIS.

EIS is a powerful technique used to analyze the electrochemical properties of systems by measuring their impedance across a range of frequencies. In EIS, a small-amplitude alternating current voltage is applied to the system, and the resulting current response is recorded. The results are commonly presented as Nyquist plots, which depict the real and imaginary components of impedance, offering insights into the charge transfer resistance (R_{ct}) and the double-layer capacitance (C_{dl}) at the electrode/electrolyte interface.[30] In addition, EIS enables the characterization of various electrochemical processes including charge transfer, diffusion, and adsorption, occurring at different timescales. Accordingly, the EIS is particularly advantageous for studying the intrinsic properties of electrode materials or specific processes that could influence conductance, resistance, or capacitance in electrochemical systems, by analyzing the impedance response over a broad frequency range. Accordingly, all nanomaterials were characterized and screened either through considering the redox behaviors of the targeting analyte (nitro-aromatic group), or through analyzing the redox reactions of the standard redox species (10 mM of ($K_3[Fe(CN)_6]$)). In both cases, redox reaction(s) and the generated cathodic current of nitroaromatic groups was considered as the main evaluation criteria for the nanomaterial selection. Moreover, EIS generated Nyquist plots were analyzed and taken into consideration to identify the best nanocomposite assigned for the fabrication of TNT-sensor.

As shown in Fig. 3a, strong reduction peak currents, higher than the unmodified electrode, were produced by all modified electrode surfaces with the metal oxides nanomaterials. These reduction peaks were corresponding to the direct voltammetric signals generated from the TNT redox reactions. Among all tested metal oxides, MnO_2 and Co_3O_4 modified-SPE provided the highest reduction voltammetric signal for the three-nitro aromatic groups. Accordingly, MnO_2 and Co_3O_4 were selected as the basic sensor components to be conjugated with the carbon nanotubes for higher conductivity as well as electro–catalytic activity. Accordingly, an almost 5-fold increase in the electrochemical signal of TNT was achieved when the modified SPE with the Co_3O_4–MnO_2@MWCNTs was employed for nitro aromatic reduction, as shown in Fig. 3b. Electrode surface modification with the nanocomposite (Co_3O_4–MnO_2@MWCNTs) strongly supported the voltammetric responses towards the TNT redox reactions due to the synergistic catalytic effect and faster electron transfer.

Moreover, modified electrodes with the nanocomposite were used to study the influence of scan rate on shifting the TNT-peak positions or/and increasing the voltammetric peak current, as shown in Fig. 3c and e. In this respect, adsorption-controlled process or electrode-diffusion controlled process could be identified from the scan rate effect. Thus, consecutive cyclic voltammetric measurements of the TNT were carried out over a range of scan rates, while the other experimental parameters (*e.g.* potential range, electrolytes, pH, and deposition time) are kept constant. The reduction peak height of the TNT was continuously increased with increasing the scan rate from 20 to 110 mV s^{-1} (as shown in Fig. 3c). From the obtained and presented results in this figure, the square root of the scan rate (*X*-axis) was plotted *vs.* the increase in the reduction current (*Y*-axis), *i.e.* ($v^{1/2}$ *vs.* i_p), Fig. 3d. In parallel, a systematic shift in the reduction peak position with scan rate in cyclic voltammetric measurements was obtained in Fig. 3e. As a result, the cathodic peak current provided a good linearity with the square root of scan rate, confirming that a diffusion-controlled process dominates nitro aromatic reduction.

In addition, the electrochemical characterization, including CV and EIS, revealed well-defined and sharp reversible redox peaks, and the low charge transfer resistances highlighting the role of metal oxides in enhancing electrochemical signals and reducing overall charge transfer and diffusion resistances, as shown in Fig. 4a and b.

The materials were tested for the reversible reaction of the ferricyanide in 10 mM PBS, and distinct behaviors were observed. All metal oxides exhibited stronger electrochemical performance compared to the bare SPE. Among the modified electrodes, MnO_2 and Co_3O_4 exhibited the highest peak current, suggesting enhanced electron transfer capability and catalytic activity Fig. 5a. The Nyquist plots (Fig. 4b) provide insights into the charge transfer resistance (R_{ct}) of the modified SPEs. The bare SPE displayed a large semicircle, indicating high charge transfer resistance, which is a drawback and undesirable electrochemical sensing features. Among metal oxides, MnO_2 and Co_3O_4 exhibited the smallest semicircles, indicating lower R_{ct} and superior conductivity.

The CV results (Fig. 4c) demonstrated significant differences in electrochemical activity among the modified electrodes with MWCNTs. The bare SPE exhibited the lowest peak currents, while other electrodes upon modification displayed enhanced redox activity, with CNTs-based electrodes showing the highest current responses. Notably, the Co_3O_4–MnO_2@MWCNTs-based surfaces exhibited the highest redox peak current, indicating a strong synergistic effect between the CNTs and the hybrid bimetal oxides (Co_3O_4 and MnO_2). In addition, the Nyquist plots (Fig. 4d) further confirm the differences in generated R_{ct} among the modified electrodes. Thus, the Co_3O_4–MnO_2@MWCNTs-based electrodes exhibited the smallest semicircle, signifying the lowest charge transfer resistance and fastest electron transfer kinetics. Finally, the effect of scan rate was investigated utilizing ferricyanide as the standard redox probe, showing

 © 2025 The Author(s). Published by the Royal Society of Chemistry

Open Access Article. Published on 29 July 2025. Downloaded on 2/19/2026 11:39:10 AM.
This article is licensed under a Creative Commons Attribution-NonCommercial 3.0 Unported Licence.

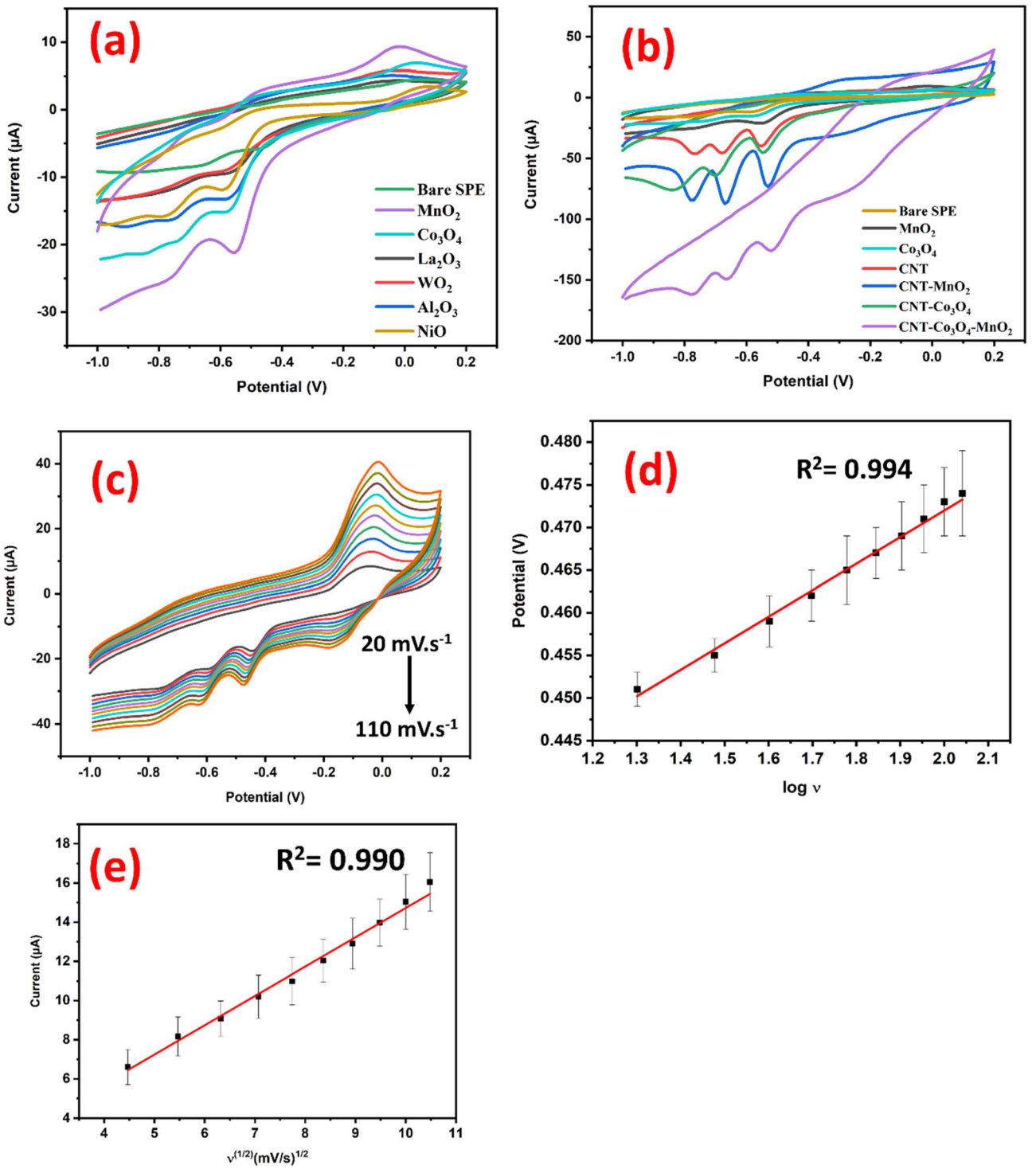

Fig. 3 (a) TNT (1.6 ppm) cyclic voltammetric reaction(s) at unmodified (bare) and modified SPEs with different metal oxides (MnO_2, WO_3, Co_3O_4, Al_2O_3, La_2O_3, and NiO). (b) TNT cyclic voltammetric reaction(s) at bare, MnO_2, Co_3O_4, MWCNTs, MnO_2-MWCNTs, Co_3O_4-MWCNTs and MnO_2–Co_3O_4@MWCNTs. (c) TNT cyclic voltammetric reaction(s) using the MnO_2–Co_3O_4@MWCNTs-based electrode at different scan rates. (d) TNT reduction peak potential value *versus* the square root of scan rates. (e) The calibration plot of the cathodic current *versus* the scan rate$^{1/2}$. The voltammetric experiments were carried out in a phosphate buffer (pH 6.5, 10 mM).

a linear increase in peak current with increasing the scan rates. This confirms that the reversible redox reaction of FCN occurring at the electrode surface is diffusion-controlled and influenced by the scan rate, as demonstrated in Fig. 4(e and f).

Interestingly, the total number of electron transfer involved in the redox reactions of TNT at the modified electrode surface was calculated from the given Laviron equation:

$$E_p = E_0' + (RT/\alpha nF)\log(RTk_0/\alpha nF) + (RT/\alpha nF)\log \nu$$

Open Access Article. Published on 29 July 2025. Downloaded on 2/19/2026 11:39:10 AM.
This article is licensed under a Creative Commons Attribution-NonCommercial 3.0 Unported Licence.

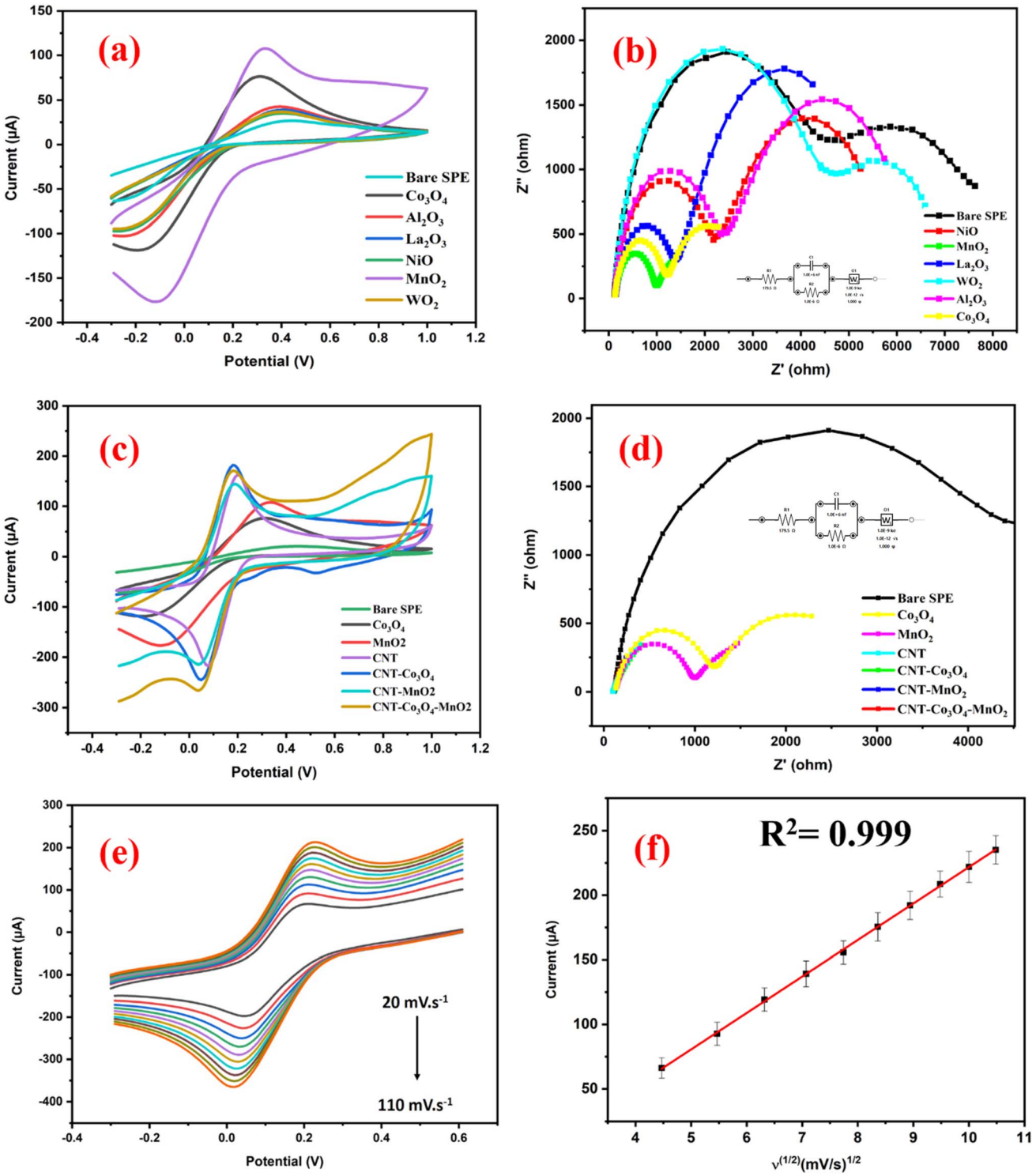

Fig. 4 (a) Voltammetric characterization for the modified screen-printed electrodes with metal oxides (MnO_2, WO_3, Co_3O_4, Al_2O_3, La_2O_3, and NiO) (b) Impedimetric characterization (Nyquist plots) for the modified screen-printed electrodes with metal oxides nanostructures (c) CVs of 10 mM FCN voltammetric signals of bare, MnO_2, Co_3O_4, CNTs, CNTs-MnO_2, CNTs-Co_3O_4, and Co_3O_4–MnO_2@MWCNTs modified SPEs. (d) The corresponding Nyquist plots of bare and the modified electrodes. The inset in (b and d) is the equivalent Randles-circuit used for data fitting. (e) Effect of scan rate changes (from 20.0 to100 mV s^{-1}) on the voltammetric signals (*f*) the corresponding calibration plot of peak current *vs.* the scan rate$^{1/2}$.

© 2025 The Author(s). Published by the Royal Society of Chemistry

Open Access Article. Published on 29 July 2025. Downloaded on 2/19/2026 11:39:10 AM.
This article is licensed under a Creative Commons Attribution-NonCommercial 3.0 Unported Licence.

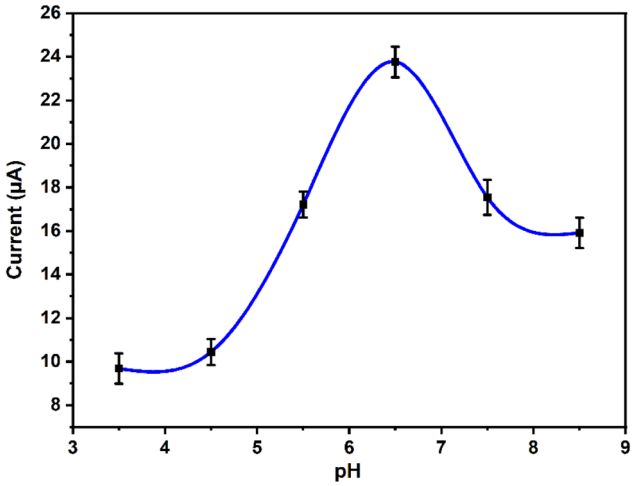

Fig. 5 pH effect on the voltammetric reduction of TNT using the Co_3O_4–MnO_2@MWCNTs-based electrode.

where F is the Faraday's constant (96.485 C mol^{-1}), n is the number of electrons participating in the TNT reduction, α is the coefficient of electron transfer, T is the temperature of electrochemical cell (298.15 K), R is the standard the universal gas constant (8.314 J mol^{-1} K^{-1}), and $E_0^{'}$ is the standard electrode potential (V). According to the slope between the log v and E_p, αn was calculated to be 0.82. Therefore, n was estimated to be 5.7 $\approx$ 6 electrons for the TNT.

3.3. Electrochemical reduction mechanism of 2,4,6-trinitrotoluene (TNT)

Voltammetric reduction of TNT typically occurs in multiple steps, involving the reduction of nitro groups on the aromatic ring. This process can occur at the Co_3O_4–MnO_2@MWCNTs-based electrode surface when TNT is reduced by gaining electrons in a cathodic process.[31] Each of the cathodic peaks reflects the individual reduction of an acceptor –NO_2 group according to the mechanism shown in Scheme 2. Six protons ($6H^+$) and six-electron ($6e^-$) transfer are required to complete the reduction of one nitro group to the amino group. The mechanism could be elaborated in three steps, which indicates the existence of two intermediates. Starting with the reduction of ortho-NO_2 group reduction (E_{red1}) is the most common mechanism for the TNT reduction mechanism. In the next step, the second nitro moiety in ortho-position (E_{red2}) will be reduced. In the last reduction step, the third para-nitro group will be eventually reduced. Subsequently, 6-protons and 6-electron transfer are needed for each –NO_2 group to be converted to a –NH_2.

Hence, the complete voltammetric reduction process of the TNT needs 18 protons and 18 electrons to produce the (2,4,6-triaminotoluene). Initially, the first reduction step starts by transferring $1H^+$ and $1e^-$, which are originating from the electrolyte sources. Consequently, TNT-H^+ is produced as an instable neutral radical. Accompanied by the next transfer of $1H^+$ and $1e^-$ (oxygen is attached to the proton of the intermediate). Consequently, -nitroso-intermediate is produced, and water molecule is removed. Successively, protonation of the hydroxylamine is obtained. Finally, the next $2e^-/2H^+$ reduction leads to the creation of an amine group, where all nitro groups are reduced to amino group (–NH_2).

3.4. Effect of pH

The effect of pH (Fig. 5) on the reduction peak currents of TNT (3.3 ppm) was investigated using phosphate buffer solution in PBS (10 mM), with six different pH values (3.5, 4.5, 5.5, 6.5, 7.5, and 8.5), and at a scan rate of 50 mV s^{-1}. As the pH increased from 3.5 to 6.5, the sensing performances was improved until exceeding the values of pH 6.5. The corresponding curves obtained by CV at different pH values showed that the highest voltammetric reduction of the TNT is obtained at pH = 6.5.

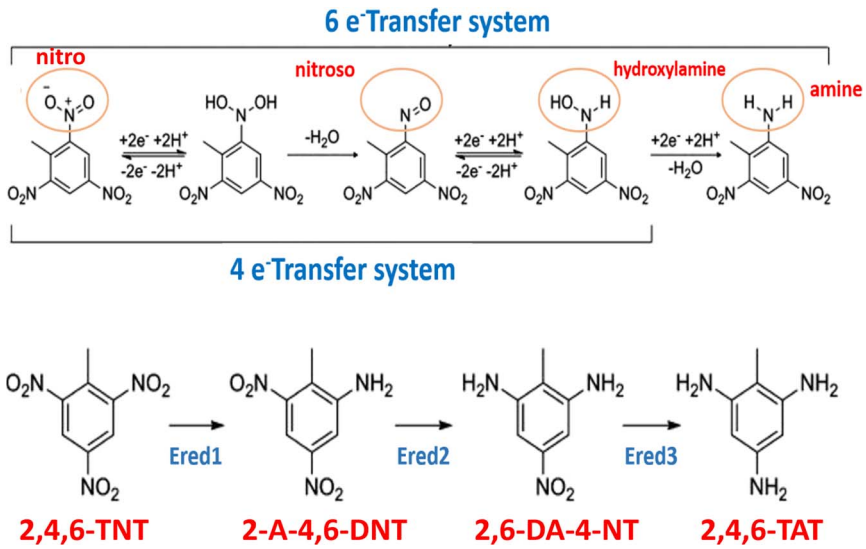

Scheme 2 Demonstrated the most common two reaction mechanisms for the reduction of TNT explosives in aqueous solution. Reproduced from the study by Chu *et al.*[31]

Open Access Article. Published on 29 July 2025. Downloaded on 2/19/2026 11:39:10 AM. This article is licensed under a Creative Commons Attribution-NonCommercial 3.0 Unported Licence.

3.5. TNT quantification using DPV

DPV is an effective quantitative voltammetric technique used to provide high sensitivity and low detection limit for soluble reactive redox species. Here, DPV experiments were performed for the determination of trace amounts of TNT under the optimum conditions. DPV readouts were conducted in the phosphate buffer solution (pH 6.5), and scan rate was 50 mV s^{-1}. Accordingly, DPV responses were collected for a series of standard solutions of TNT (concentration range from 0.33 to 50 ppm), while the calibration curve was constructed, as shown in Fig. 6. The peak current of TNT displayed a linear relation with the regression coefficient (R^2 = 0.982). The LOD and LOQ for the TNT were calculated from the calibration curves to be 0.153 ppm, and 0.466 ppm, respectively. The obtained analytical characteristics were compared with previously reported electrochemical methods. As presented in Table 1, the newly developed TNT-sensor supported by the optimized voltammetric assay exhibited high sensitivity, with low LOD value, to be an added value to the previously reported electrochemical systems developed for TNT detection.

3.6. Selectivity, stability and sensor reproducibility

Selectivity is one of the most important metrics to evaluate the performance of Co_3O_4–MnO_2@MWCNTs/SPE towards the targeting analytes in presence of other foreign (non-targeting) molecules. Accordingly, electrochemical responses to a series of nitroaromatic compounds, including nitrobenzene (NB), 2,4-dinitrotoluene (2, 4-DNT), and 2,4,6, trinitrotoluene were investigated. The generated/produced number of cathodic peaks are correlated with the active number of nitro-groups present in the tested nitroaromatic compounds. Therefore, the NB exhibited only one reduction current peak at −0.64 V. Meanwhile, 2,4-DNT and exhibited two reduction peaks at −0.70 V, and −0.53 V. While, TNT showed three electrochemical reduction peaks at −0.38 V, −0.55 V, and −0.68 V (as shown in Fig. 7A).

Remarkably, the TNT voltammetric detection could be achieved here with high selectivity through tracking the changes in the peak heights of the distinguished cathodic peak appeared at −0.38 V. Correspondingly, the interference of two common explosives (1,3,5-trinitro-1,3,5-triazinane(RDX), [3-nitrooxy-2,2-bis(nitrooxymethyl)propyl] nitrate (PETN)) and several common substances in the environment (boric acid, ammonium nitrate, diphenylamine, sodium azide, potassium perchlorate, and ammonium chromate) on TNT detection was explored (Fig. 7B). Due to high selectivity towards the TNT obtained by the newly developed-sensor surface, testing different non-targeting explosive compounds did not show cross-

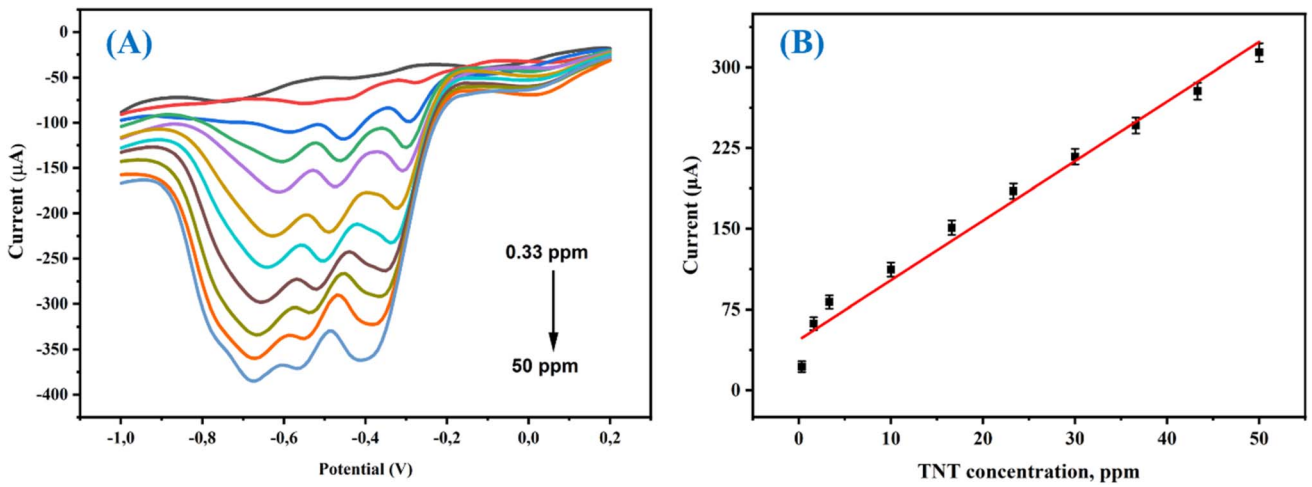

Fig. 6 (A) DPV for different concentrations of TNT on Co_3O_4–MnO_2@MWCNTs-based electrode. TNT concentration range: 0.33–50 ppm; (B) linear relationship between peak current ratio and TNT concentration.

Table 1 TNT electrochemical detection reported methods using different modified working electrodes. The newly developed DPV method is included for comparison

Modified electrode	Analytical technique	Linear range	LOD	Ref.
Graphene or hydrogenated graphene/GCE	CV, DPV	1.0–20 ppm	400 ppb	32
Gold nanoparticles and a poly(ophenylenediamine–aniline) film/GCE	CV	2.5–40 ppm	2.1 ppm	33
Electrochemically exfoliated graphene sheets/GCE	CV, DPV	—	6.74 ppm	34
TiO_2/nano-Pt particles/GCE	CV	1.0–15 ppm	200 ppb	35
Pt-nanoparticle (NP) ensemble-on-graphene hybrid nanosheet/GCE	CV	0.5–40 ppm	3.0 ppm	36
Silver nanoparticles/carboxylic sodium groups/GCE	CV	1.0–70 ppm	0.45 ppm	37
Carbon fiber microelectrode	SWV	—	0.4 ppm	38
Graphene nanoribbons or graphite microparticles/GCE	SWV, DPV	1.0–19 ppm	1.0 ppm	39
Co_3O_4–MnO_2@MWCNTs/SPE	CV, DPV	0.33 to 50 ppm	0.15 ppm	This work

© 2025 The Author(s). Published by the Royal Society of Chemistry

Open Access Article. Published on 29 July 2025. Downloaded on 2/19/2026 11:39:10 AM.
This article is licensed under a Creative Commons Attribution-NonCommercial 3.0 Unported Licence.

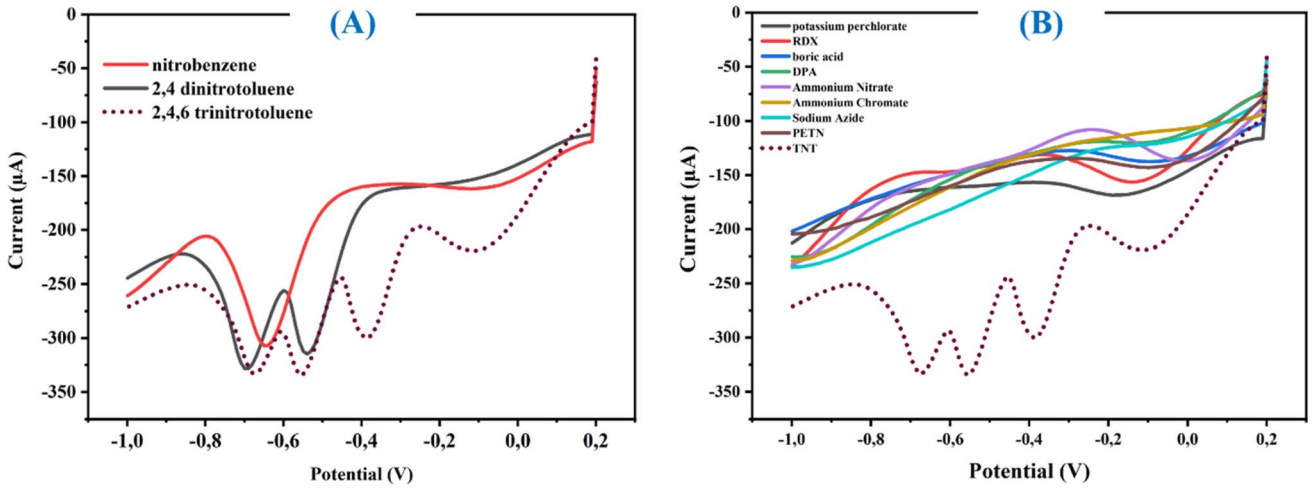

Fig. 7 (A) Nitroaromatic compounds (nitrobenzene, 2,4-dinitrotoluene, 2,4,6-trinitrotoluene). (B) Most common interfering compounds.

reactivity or negative impact on the TNT voltammetric signals. Furthermore, no significant effects were obtained from other environmental substances. Hence, the selectivity features acquired by the TNT-sensor is attributed to the utilization of Co_3O_4–MnO_2@MWCNTs nanocomposite as a new electrode surface modifier. Moreover, no significant changes in the voltammetric responses of TNT was obtained when a mixture of the non-targeting substances was tested.

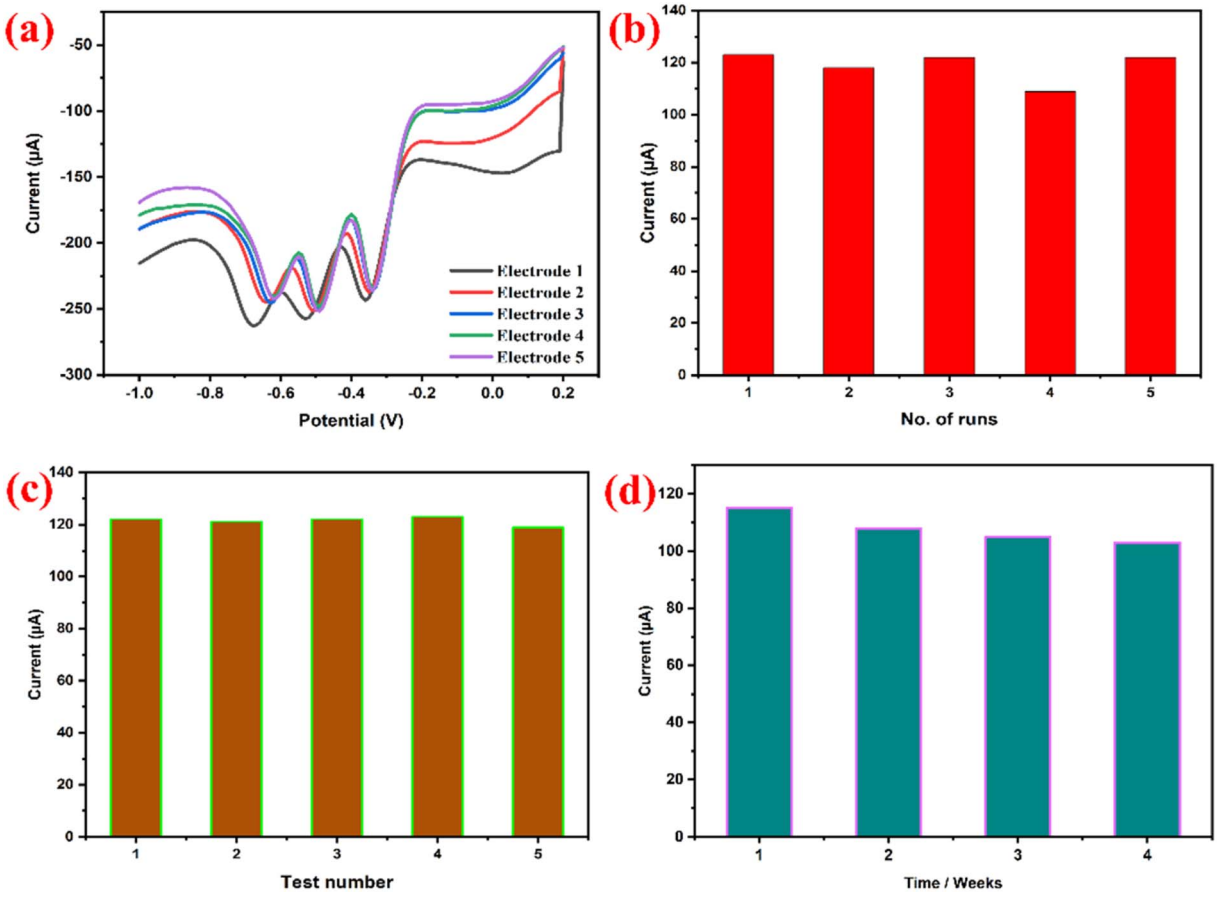

Fig. 8 (a and b) repeatability testing of the Co_3O_4–MnO_2@MWCNTs/SPE performed by DPV in 10 mM PBS with 30 ppm of the TNT; (c) reproducibility test of the Co_3O_4–MnO_2@MWCNTs/SPE performed by DPV in 10 mM PBS with 30 ppm TNT (d) sensor stability and its lifetime.

© 2025 The Author(s). Published by the Royal Society of Chemistry

Open Access Article. Published on 29 July 2025. Downloaded on 2/19/2026 11:39:10 AM. This article is licensed under a Creative Commons Attribution-NonCommercial 3.0 Unported Licence.

Table 2 Determination of TNT in different real samples (tap water, ground water, sand, and soil) using the newly optimized DVP assay, and the developed sensor surface

Sample	Added TNT (ppm)	Detected TNT (ppm)	Recovery (%)
Tap water	4.97	4.99	100.4
Ground water	4.97	4.74	95.3
Sand	4.97	4.69	94.3
Soil	4.97	4.78	96.1

To verify the feasibility and repeatability, repeated measurements were carried out using a single electrode-chip (Fig. 8a and b). The experimental data outcomes of five repeated tests showed a slight change in current intensity (fluctuated with less than 5.0%), while no shifting in the cathodic peak positions was obtained. These findings revealed the remarkable durability and readiness of TNT-based electrodes.

On the other hand, the reproducibility of the modified electrodes was demonstrated (Fig. 8c) by comparing the detection performance of TNT using five-individual modified chips with the nanocomposite. The results showed that the all tested electrodes exhibited high stability, having an RSD of 1.24%, further implying the practicability of those chips and their stable surface modification.

Finally, stability of the TNT-sensor chips and their lifetime were investigated over several weeks from their fabrication, as shown in Fig. 8d. About 6.0% deviation in peak current was obtained, displaying the high stability of the sensor's fabrication/modification. The DPV responses of TNT (30 ppm) were collected using a single sensor chip for multiple measurements in four different weeks. All optimal parameters were applied.

3.7. The use of TNT-based sensor for real sample analysis

To verify the TNT-sensor's suitability for real-applications, TNT-sensing performance and its analytical reliability were evaluated in complex matrices (tap water, ground water, sand, and soil samples). Thus, determination of TNT in different environmental samples was established by applying the standard addition method. The standard addition method was adopted with addition of 4.97 ppm of TNT in untreated tap water, ground water and suspended sand and soil samples in 10 mM PBS (pH 6.5). When the samples were spiked with TNT (4.95 ppm), the sensor presented good recovery rates ranging from 94.3% to 100.4% (Table 2). This result indicated that the optimized DVP assay alongside the modified sensor surface enabled high practicability, reliability, and efficiency.

4. Conclusion

A novel electrochemical sensor for TNT detection was successfully developed using a screen-printed electrode (SPE) modified with a Co_3O_4–MnO_2@MWCNTs nanocomposite. The use of this nanocomposite significantly improved the sensor's performance due to the synergistic effects of its components. Co_3O_4 and MnO_2 provided high electrocatalytic activity, while MWCNTs offered high conductivity, mechanical stability and expandable surface area, leading to better electron transfer kinetics and reduced charge transfer resistance. During the voltammetric assay optimization, several regulating parameters were studied, and optimized. A full electrochemical mechanism was proposed for the electrochemical reduction of TNT at the modified electrode, involving the multi-step reduction of the nitro groups.

The optimized DVP assay alongside the modified SPE demonstrated a wide linear detection range for TNT (0.33 to 50 ppm) with a low detection limit of 0.153 ppm, making it suitable for trace-level detection. This LOD is competitive with other reported electrochemical TNT sensors. Additionally, the sensor exhibited good selectivity for TNT against common interferents and other nitroaromatic compounds. The distinct reduction peaks of TNT allowed for selective detection. The modified SPE showed satisfactory stability and reproducibility, crucial for practical applications. Thus, this sensing platform holds promise for on-site and real-time TNT detection in environmental and security applications due to its rapid response, sensitivity, selectivity, and stability. The use of SPEs makes the sensor potentially low-cost and disposable.

Data availability

The reported data of this manuscript is available upon request from the corresponding authors.

Conflicts of interest

The authors declare that there are no conflicts of interest regarding the publication of this manuscript.

References

1 V. Shvalya, J. Olenik, D. Vengust, J. Zavašnik, J. Štrbac, M. Modic, O. Baranov and U. Cvelbar, *J. Hazard. Mater.*, 2024, **476**, 135171.
2 H. M. Junaid, M. T. Waseem, Z. A. Khan, H. Gul, C. Yu, A. J. Shaikh and S. A. Shahzad, *J. Photochem. Photobiol., A*, 2022, **428**, 113865.
3 E. Aznar-Gadea, P. J. Rodríguez-Canto, J. P. Martínez-Pastor, A. Lopatynskyi, V. Chegel and R. Abargues, *ACS Appl. Polym. Mater.*, 2021, **3**, 2960–2970.
4 J. S. Strehse, M. Brenner, M. Kisiela and E. Maser, *Arch. Toxicol.*, 2020, **94**, 4043–4054.
5 E. A. Naumenko, B. Ahlemeyer and E. Baumgart-Vogt, *Environ. Toxicol.*, 2017, **32**, 989–1006.
6 S. Masoumi, H. Hajghassem, A. Erfanian and A. Molaei Rad, *Sens. Rev.*, 2016, **36**, 414–420.
7 A. Arman, Ş. Sağlam, A. Üzer and R. Apak, *Talanta*, 2022, **238**, 122990.
8 X. Zhang, Y. Luo, L. Xia, Y. Song, W. Li, L. Kong, Y. Liu, C. Shen, C. Huang and Y. Chu, *Talanta*, 2025, **281**, 126857.

© 2025 The Author(s). Published by the Royal Society of Chemistry

Open Access Article. Published on 29 July 2025. Downloaded on 2/19/2026 11:39:10 AM. This article is licensed under a Creative Commons Attribution-NonCommercial 3.0 Unported Licence.

9 C. E. Son, H. R. Choi and S. S. Choi, *Rapid Commun. Mass Spectrom.*, 2023, **37**, e9645.
10 T. H. Bünning, J. S. Strehse, A. C. Hollmann, T. Bötticher and E. Maser, *Toxics*, 2021, **9**, 60.
11 J. A. Threadgold, P. E. Fowler and G. A. Eiceman, *Anal. Chem.*, 2024, **96**, 13830–13837.
12 K. K. Gulati, V. Gambhir and M. Reddy, *Def. Sci. J.*, 2017, **67**, 588–591.
13 W. Gao, T. Wang, C. Zhu, P. Sha, P. Dong and X. Wu, *Talanta*, 2022, **236**, 122824.
14 A. K. Jamil, E. L. Izake, A. Sivanesan and P. M. Fredericks, *Talanta*, 2015, **134**, 732–738.
15 Y. Ma, S. Wang and L. Wang, *TrAC, Trends Anal. Chem.*, 2015, **65**, 13–21.
16 L. Zhen, N. Ford, D. K. Gale, G. Roesijadi and G. L. Rorrer, *Biosens. Bioelectron.*, 2016, **79**, 742–748.
17 S. Content, W. C. Trogler and M. J. Sailor, *Chem.–Eur. J.*, 2000, **6**, 2205–2213.
18 R. T. Echols, M. M. Christensen, R. M. Krisko and J. H. Aldstadt, *Anal. Chem.*, 1999, **71**, 2739–2744.
19 B. Boulesnam, F. Hami, D. Trache and T. A. Zaid, *ENP Eng. Sci. J.*, 2021, **1**, 75–83.
20 S. M. Ünsal and E. Erkan, *Turk. J. Chem.*, 2022, **46**, 923–928.
21 R. Song, J. Zhang, G. Yang, Y. Wu, J. Yu and H. Zhu, *Sensors*, 2024, **24**, 2043.
22 R. Y. A. Hassan, *Journal*, 2022, 22.
23 N. Sultana, S. Upadhyaya and N. S. Sarma, in *Nanoscale Matter and Principles for Sensing and Labeling Applications*, Springer, 2024, pp. 73–93.
24 H. S. Magar, E.-s. M. Duraia and R. Y. A. Hassan, *Sci. Rep.*, 2025, **15**, 11229.
25 H. S. Magar, A. M. El Nahrawy, R. Y. A. Hassan and A. B. Abou Hammad, *RSC Adv.*, 2024, **14**, 34948–34963.
26 N. Rajab, H. Ibrahim, R. Y. A. Hassan and A. F. A. Youssef, *RSC Adv.*, 2023, **13**, 21259–21270.
27 P. Li, X. Li and W. Chen, *Curr. Opin. Electrochem.*, 2019, **17**, 16–22.
28 M. Bilal, A. R. Bagheri, P. Bhatt and S. Chen, *J. Environ. Manage.*, 2021, **291**, 112685.
29 M. Ahmed, S. Ahmad, T. Nawaz, M. A. Durrani, A. Ali, S. Saher, M. A. Z. Khan, M. Egilmez, A. Samreen and F. Mustafa, *Electrochem. Sci. Adv.*, 2022, **2**, e2100085.
30 H. S. Magar, R. Y. Hassan and A. Mulchandani, *Sensors*, 2021, **21**, 6578.
31 C. K. Chu, M. Pumera and L. R. Rulisek, *J. Phys. Chem. C*, 2012, **116**, 4243–4251.
32 T. H. Seah, H. L. Poh, C. K. Chua, Z. Sofer and M. Pumera, *Electroanalysis*, 2014, **26**, 62–68.
33 Ş. Sağlam, A. Üzer, Y. Tekdemir, E. Erçağ and R. Apak, *Talanta*, 2015, **139**, 181–188.
34 Y. T. Yew, A. Ambrosi and M. Pumera, *Sci. Rep.*, 2016, **6**, 33276.
35 B. Filanovsky, B. Markovsky, T. Bourenko, N. Perkas, R. Persky, A. Gedanken and D. Aurbach, *Adv. Funct. Mater.*, 2007, **17**, 1487–1492.
36 S. Guo, D. Wen, Y. Zhai, S. Dong and E. Wang, *ACS Nano*, 2010, **4**, 3959–3968.
37 X. Lu, H. Qi, X. Zhang, Z. Xue, J. Jin, X. Zhou and X. Liu, *Chem. Commun.*, 2011, **47**, 12494–12496.
38 X. Fu, R. F. Benson, J. Wang and D. Fries, *Sens. Actuators, B*, 2005, **106**, 296–301.
39 M. S. Goh and M. Pumera, *Anal. Bioanal. Chem.*, 2011, **399**, 127–131.

© 2025 The Author(s). Published by the Royal Society of Chemistry